Correlation analysis of the beam angle dependence for elastography

Min Rao and Tomy Varghese[a)]
Department of Medical Physics, The University of Wisconsin-Madison, 1300 University Avenue, 1530 MSC, Madison, Wisconsin 53706

(Received 10 November 2005; revised 17 March 2006; accepted 20 March 2006)

Signal decorrelation is a major source of error in the displacements estimated using correlation techniques for elastographic imaging. Previous papers have addressed the variation in the correlation coefficient as a function of the applied compression for a finite window size and an insonification angle of zero degrees. The recent use of angular beam-steered radio-frequency echo signals for spatial angular compounding and shear strain estimation have demonstrated the need for understanding signal decorrelation artifacts for data acquired at different beam angles. In this paper, we provide both numerical and closed form theoretical solutions of the correlation between pre- and post-compression radio-frequency echo signals acquired at a specified beam angle. The expression for the correlation coefficient obtained is a function of the beam angle and the applied compression for a finite duration window. Accuracy of the theoretical results is verified using tissue-mimicking phantom experiments on a uniformly elastic phantom using beam-steered data acquisitions on a linear array transducer. The theory predicts a faster decorrelation with changes in the beam or insonification angle for longer radio-frequency echo signal segments and at deeper locations in the medium. Theoretical results provide useful information for improving angular compounding and shear strain estimation techniques for elastography.
 [DOI: 10.1121/1.2195290]

PACS number(s): 43.80.Qf [TDM] Pages: 4093–4101

I. INTRODUCTION

Elastography, a method for imaging the tissue stiffness, has gained interest for the diagnosis of disease in recent years.[1–16] This method estimates local strains typically in the direction of compression by computing the gradient of shifts in echo arrival times after a quasistatic tissue compression. The echo shifts or tissue displacement are computed using a one-dimensional gated cross-correlation analysis of the pre- and post-compression radio-frequency (RF) signals, with overlapping windows to improve resolution. Recent reports have presented approaches that estimate both the normal and shear strains in elastography.[16,17] However, the distortion of the echo signal as a result of the applied compression introduces decorrelation noise, which is a major source of error in strain imaging.[3,4]

Many algorithms have been developed to reduce decorrelation noise and to improve the elastographic signal-to-noise ratio (SNRe), such as temporal stretching,[18–20] multi-compression averaging,[21] and wavelet denoising.[22] Spatial-angular compounding for elastography was recently introduced by our group[23–25] to reduce noise artifacts in the resulting compounded elastograms. This method averages multiple weighted angular strain estimates around the same region-of-interest (ROI) acquired from different beam insonification angles. Elastograms generated from the pre- and post-compression signals acquired at these different beam angles are referred to as angular elastograms. However, as previously described,[24,25] when the ultrasound beam is steered away from the direction of compression, the angular elastograms suffer from larger echo signal decorrelation in the pre- and post-compression RF echo signals, when compared to the nonsteered condition, where the data acquisition and the direction of compression are the same. To investigate and optimize the performance of spatial-angular compounding for elastography, it would be helpful to have a priori knowledge regarding the noise properties of the compounded angular elastograms. The correlation coefficient has been utilized previously to ascertain the degree of signal decorrelation and to quantify improvements in strain imaging performance. In this paper, a theoretical formulation is therefore developed to account for the increased signal decorrelation between the pre- and post-compression RF signals acquired when the ultrasound beam is at a different angle with respect to the direction of compression.

To measure the performance of the cross correlation based strain estimator, a large amount of theoretical work has been reported in the literature to calculate the correlation coefficient between the pre- and post-compression RF signals.[26–30] The correlation coefficient with motion compensation due to the axial deformation of elastic tissue was derived by Meunier and Bertrand[26] using a two-dimensional (2D) Gaussian model. Cross-correlation functions for tissue like media that exhibit deterministic and stochastic strain profiles were derived by Bilgen and Insana.[27] To study the degradation in the elastographic image quality due to the lateral and elevational motion of the scatterers, a 3D model was proposed by Kallel and Ophir[28] for predicting the correlation coefficient using separable point-spread functions in

[a)]Author to whom correspondence should be addressed. Electronic mail: tvarghese@wisc.edu

the axial, lateral, and elevational directions, respectively. An expression for the correlation coefficient that depends on both the applied compression and the finite size of the window used for the cross-correlation processing was developed by Varghese *et al.*[29] This formulation accounted for the intrawindow signal decorrelation due to the applied compression. The performance of the standard cross correlation approach used to estimate the complex motions and the resulting deformations in 3D was investigated by Bilgen.[30] However, all these models assume that the compression and ultrasound beam are along the same direction, and therefore are not suitable to compute the correlation coefficient for angular elastograms obtained by beam steering.

Many studies have also been performed to investigate spatial correlations in ultrasound speckle pattern motion in medical ultrasonic images.[31–35] All of these prior studies were directed toward B-mode image compounding, where the theories developed studied correlations between echo signals acquired from the same spatial location but different insonification angles to reduce speckle noise artifacts in the B-mode images. The analysis was recently extended by Chen *et al.*[36] to study the correlation of RF signals that intersect at the same spatial location obtained from different angular insonifications. This formulation is useful in evaluating the improvement in parametric images of the scatterer size or attenuation coefficient with spatial angular compounding, since these parameters are estimated from the angular RF data. Since the contribution of the insonification angle was addressed in these models we have modified this approach to investigate angular compounding for elastography by including the applied compression and the use of a finite sized processing window.

In this paper, initially following the framework used by Chen *et al.*,[36] a closed form expression is derived for the correlation coefficient between pre- and post-compression RF signals acquired at specific beam angles. To corroborate the theoretical development, experimental results using a tissue-mimicking phantom are presented that verify and validate the theoretical expressions. Factors that affect the signal decorrelation versus the beam angle are discussed. Both the rigorous numerical derivation and the closed form expressions for the correlation coefficient can be used to predict the rate of signal decorelation in the angular elastograms and provide a clear understanding of the performance of angular compounding techniques in elastography.

II. THEORY

Ultrasonic RF echo signals before and after compression is modeled by

$$s_1(x,z) = P(x,z) \otimes T(x,z),$$

$$s_2(x,z) = P(x,z) \otimes T(x,az), \tag{1}$$

where the subscripts 1 and 2, specify the pre- and post-compression echo signals obtained from an elastic tissue medium, $T(x,z)$ denotes the tissue scattering function, and $P(x,z)$ is the pulse-echo point-spread function (PSF) of the imaging system. The symbol $\otimes$ denotes the convolution operation. The parameter a is the compression or strain factor that scales the tissue scattering function defined in terms of the actual applied tissue strain ε, $a=1/(1-\varepsilon)\sim 1+\varepsilon$ for $\varepsilon \ll 1$. Here a 2D model is used because the ultrasound beam in currently available transducers is much wider in the elevational direction compared to the lateral direction. Thus, the scatterer movement in the elevational direction does not cause significant loss of coherence in the echoes.

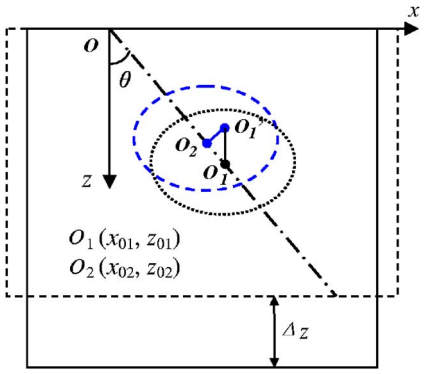

FIG. 1. (Color online) Schematic diagram illustrating the acquisition of pre- and post-compression RF signals with a beam steering angle θ. The precompression RF signals are obtained from scatterers at position O_1, while the post-compression signals are obtained from the corresponding scatterers at location O_2.

There are several models that define the $T(x,z)$ term. To simplify the tissue model, we assume a large number of very small inhomogeneities (Rayleigh scatterers) with respect to the wavelength of the PSF[26]

$$T(x,z) = \sum_i T_i \delta(x - x_i, z - z_i), \tag{2}$$

where $\delta(x,z)$ is the 2D Dirac or impulse function, (x_i,z_i) denotes the randomly distributed centers of each inhomogeneity, and T_i the echogenicity of each scatterer. The scatterer distribution is assumed to be δ correlated, which means the correlation length of scatterers is very short compared to the acoustic wavelength of the transmit pulse.

The cumulative signal amplitude from scatterers at position O_1 (x_{01},z_{01}) in the precompression medium can be written as[31]

$$s_1 = \sum_i |T_i||P_{1,i}|\exp(j\vartheta_i). \tag{3}$$

The subscript i refers to an individual scatterer, $|P|$ is the magnitude of the pulse-echo PSF from the scatterers, and $\exp(j\vartheta)$ represents the combined phase of T and P. The phase factors in ϑ are uniformly distributed over 2π radians with zero mean. An illustration of this concept is shown in Fig. 1. We establish our coordinates by setting the position of transducer as the origin, and the beam steering angle is θ.

A quasistatic compression is then applied to the medium along the $-z$ direction, with the scatterers moving toward the transducer. For simplicity, we assume the position O_1 is at the center of the medium in the lateral direction, which implies that the scatterer movement in the lateral direction is small enough to be considered negligible. Thus, tissue scat-

terers around O_1 move to position O_1' after compression, as shown in Fig. 1. The post-compression signal is then generated from scatterers at position O_2 (x_{02}, z_{02}), which are the projection positions of O_1' on the ultrasound beam. The cumulative signal strength after compression can be written as

$$s_2 = \sum_i |T_i||P_{2,i}|\exp(j\vartheta_i)\exp(j\Delta\phi_i), \tag{4}$$

where $\Delta\phi_i$ is the phase difference between pre- and post-compression signals, which can be written as $4\pi(R_{2,i} - R_{1,i})/\lambda_0$, where λ_0 is the wavelength at the center frequency, and $R_{1,i}$, $R_{2,i}$ are the distances from the ith scatterer to the transducer for the pre- and post-compression situations, respectively,

$$R_{1,i} = \sqrt{x_i^2 + z_i^2},$$

$$R_{2,i} = \sqrt{x_i^2 + (z_i/a)^2}, \tag{5}$$

$$R_{2,i} - R_{1,i} = \frac{1 - a^2}{a^2(R_{1,i} + R_{2,i})} z_i^2.$$

The cross correlation between the signals acquired before and after compression can be written as[31]

$$\langle s_1 s_2^* \rangle = \sum_i |T_i|^2 |P_{1,i}||P_{2,i}|\exp(j\Delta\phi_i). \tag{6}$$

The 2D PSF in the focal zone of each ultrasound beam of a linear array transducer can be expressed in the following form:

$$|P(x,z)| = p_x(x)p_z(z), \tag{7}$$

where p_x represents the lateral beam spread function, and p_z represents the axial spread function. For a rectangular aperture, for example, the lateral PSF for a pulse-receive response at the focus or in the far-field can be written as

$$p_x(x) = \sin^2(\pi f_0 x)/(\pi f_0 x)^2, \tag{8}$$

where $f_0 = D/r\lambda_0$, D is the effective transducer aperture, and r is the focal distance, $r = z_{01,02}/\cos\theta$. If we assume that the ultrasound pulse transmitted by the transducer has a Gaussian envelope with characteristic width σ_z, then p_z can be expressed as

$$p_z(z) = \exp(-z^2/2\sigma_z^2). \tag{9}$$

For the i^{th} scatterer, the lateral distances to the beam axis for the pre- and post-compression cases can be written as

$$l'_{1,i} = (x_i - x_{01})\cos\theta - (z_i - z_{01})\sin\theta,$$

$$l'_{2,i} = (x_i - x_{02})\cos\theta - (z_i/a - z_{02})\sin\theta. \tag{10}$$

Similarly, the axial distances from the i^{th} scatterer to the center point are

$$l''_{1,i} = (x_i - x_{01})\sin\theta + (z_i - z_{01})\cos\theta,$$

$$l''_{2,i} = (x_i - x_{02})\sin\theta + (z_i/a - z_{02})\cos\theta. \tag{11}$$

Hence, the PSF for the i^{th} scatterer can be written as

$$P_{k,i} = p_x(l'_{k,i})p_z(l''_{k,i}), \quad (k = 1,2). \tag{12}$$

Substituting Eq. (12), into Eq. (6), we obtain

$$\langle s_1 s_2^* \rangle = \sum_i |T_i|^2 |p_x(l'_{1,i})||p_z(l''_{1,i})||p_x(l'_{2,i})||p_z(l''_{2,i})| \times \exp(j\Delta\phi_i). \tag{13}$$

Going to a continuous representation, x_i and z_i become x and z, and the summation becomes a 2D integral about x and z. Thus,

$$\langle s_1 s_2^* \rangle = B' \int\int |p_x(l'_1)||p_z(l''_1)||p_x(l'_2)||p_z(l''_2)| \times \exp(j\Delta\phi)dxdz, \tag{14}$$

where B' is a normalization factor. An analytical closed form solution for the above equation is difficult to obtain. Thus, it is necessary to either resort to numerical solutions or apply approximations to simplify the expression in Eq. (14).

To simplify the 2D integral in Eq. (14), we utilize a Gaussian envelope to model the lateral PSF as shown

$$p_x(x) = \exp(-x^2/2\sigma_x^2). \tag{15}$$

For small beam angles ($\theta < 10°$), $\sin\theta \ll \cos\theta$, the $\sin\theta$ term in Eqs. (10) and (11) can be ignored. The phase term $\exp[4\pi j(R_2 - R_1)/\lambda_0]$ in Eq. (14) is a function of x and z. Since only scatterers close to the region of interest contribute to the signal, we can approximate the phase term as $\exp[2\pi jz\cos\theta(1-a^2)/a^2\lambda_0]$. We can then perform the integration in the lateral and axial direction separately as discussed by Wagner *et al.*[31] and obtain

$$\langle s_1 s_2^* \rangle = B'' \int |p_z[(z - z_{01})\cos\theta]||p_z[(z/a - z_{02})\cos\theta]|\exp\left[2\pi jz\cos\theta\frac{1-a^2}{a^2\lambda_0}\right]dz, \tag{16}$$

where B'' is the integral in the lateral direction

$$B'' = \frac{\sigma_x}{\cos\theta}\sqrt{\pi}\exp\left[-\frac{1}{4}\frac{\cos^2\theta}{\sigma_x^2}(x_{01} - x_{02})^2\right]. \tag{17}$$

Equation (16) follows the notation of a Fourier transformation (FT). The cross-correlation function is therefore a FT of the multiplication of the two PSF

$$\langle s_1 s_2^* \rangle = B''[FT\{|p_z[(z - z_{01})\cos\theta]||p_z[(z/a - z_{02})\cos\theta]|\}]_{f=((1-a^2)/a^2\lambda_0)\cos\theta}, \tag{18}$$

where FT denotes the Fourier transformation operator. The correlation coefficient is defined as[27]

$$\rho = \frac{\langle s_1 s_2^* \rangle}{\sqrt{\langle s_1 s_1^* \rangle \langle s_2 s_2^* \rangle}}. \tag{19}$$

Substituting Eq. (18) into Eq. (19) and after the integration procedure we obtain

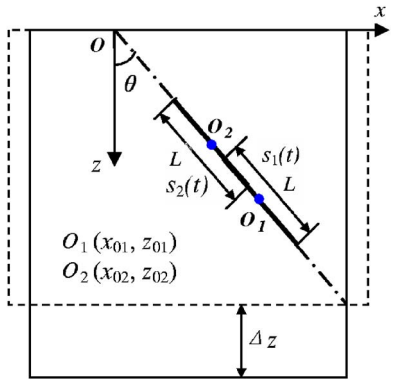

FIG. 2. (Color online) Schematic illustration of the angular RF data segment acquired before and after compression.

$$\rho = \sqrt{\frac{2a}{a^2+1}} \exp\left\{ -\frac{\cos^2\theta}{4}\left[\frac{(x_{01}-x_{02})^2}{\sigma_x^2} + \frac{(z_{01}-az_{02})^2}{\sigma_z^2} \right] \right\} \exp\left(-\frac{\sigma_z^2\pi^2 f^2}{\cos^2\theta} \right)_{f=((1-a^2)/a^2\lambda_0)\cos\theta}. \tag{20}$$

For elastographic processing, finite gated segments of the echo signal are utilized. The displacement at location O_1 is estimated from RF segments illustrated with thick lines, as shown in Fig. 2. A gated data segment is generally selected using a rectangular window. Generally, the same window is used for both pre- and post-compression data segments. Attenuation and focusing effects can be included in the window function $w(t)$, so that the intensity of $s(t)$ can be taken to be constant with depth. Thus, the correlation coefficient between the pre- and post-compression signals can be written as

$$\rho_{1,2} = \frac{\int_{t_1}^{t_2} w^2(t)\langle s_1(t)s_2^*(t)\rangle/\bar{I}dt}{\int_{t_1}^{t_2} w^2(t)dt} = \frac{\int_{-L/2}^{L/2} w^2(\xi)\langle s_1(\xi)s_2^*(\xi)\rangle/\bar{I}d\xi}{\int_{-L/2}^{L/2} w^2(\xi)d\xi} = \frac{\int_{-L/2}^{L/2} w^2(\xi)\rho(\xi)d\xi}{\int_{-L/2}^{L/2} w^2(\xi)d\xi}, \tag{21}$$

where L is the window length for the RF echo signal segment, $\bar{I}=\langle s\cdot s^*\rangle$ is the mean signal intensity. ξ is the distance from scatterers in the volume giving rise to the RF segment to the point of interest. The ρ parameter inside the integral can be either the numerical result of Eq. (14), or its approximated version in Eq. (20).

Figure 3 shows a comparison of the correlation coefficient obtained using the numerical integration of Eq. (14) and the approximated expression using Eq. (20). The following parameter values were used for the calculations: $L=3$ mm, $D=1.8$ cm, center frequency $f_c=5$ MHz with a 50% bandwidth, and $z_{01}=3$ cm. To approximate the lateral PSF, we used $\sigma_x=0.2$ mm in Eq. (15). As shown in Fig. 3, the approximated curves (dashed lines) are very close to the numerical results (solid lines) at small beam angles ($<10°$). However, the deviation of the approximated results becomes larger as the beam angle increases. This result demonstrates that the approximation is accurate only for the small beam angle, and has to be used with caution to model the decorrelation from larger beam angles.

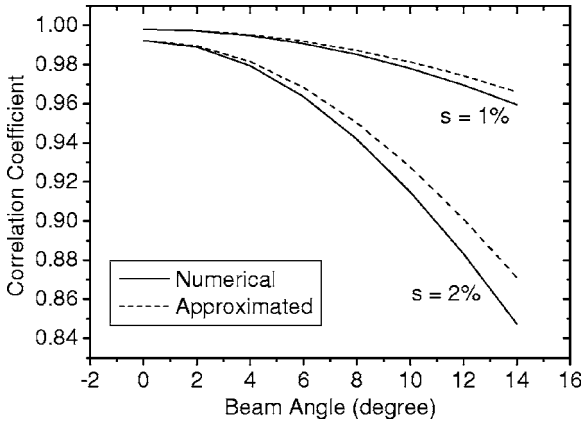

FIG. 3. Comparison between the exact numerical and approximated theoretical expression for the correlation coefficient. The correlation coefficient curves are plotted versus the beam angle.

III. EXPERIMENTAL VALIDATION

A. Method

The theoretical results derived in the previous section are verified and validated using experimental data acquired using a clinical ultrasound scanner. Pre- and post-compression RF data were obtained using a uniformly elastic tissue-mimicking phantom of size $10\times10\times10$ cm^3, manufactured in our laboratory.[37] The phantom was scanned using an Ultrasonix 500RP (Ultrasonix Medical Corporation, Bothell, WA and Vancouver, BC, Canada) real-time scanner equipped with a 5 MHz linear-array transducer with an approximate 60% bandwidth. The Ultrasonix 500RP is equipped with an ultrasound research interface (URI) that readily allows an expert programmer to alter and change the standard operating conditions and introduce new echo signal processing techniques. The Ultrasonix system setup used in our experiment enables beam steering within the angle range from −15° to 15°. In order to acquire RF data at different beam angles, we developed a URI client program, to communicate with the Ultrasonix URI and software server to control the beam steering algorithm. The URI client program enables the operator to input the maximum angle and the angular increment, and the machine will automatically scan the phantom at the specified angles during the angular sweep. In our experiment, the phantoms were scanned from 0° to 15° with a minimum angular increment of 0.75°.

The stepper motor controlled quasistatic compression of the phantom is also controlled by the URI client program on the Ultrasonix 500RP system. The program controls the stepper motor apparatus that enables synchronized acquisition of both the pre- and post-compression RF data sets after a

quasi-static compression. A compression plate with a rectangular slot fitted with the transducer was mounted on a linear stage (Velmex Inc., Bloomfield, NY) driven by a stepper motor. The compression plate is larger than the phantom surface to provide a uniform compression of the phantom. The compression was applied along the axial direction, i.e., angle 0°, without beam steering. Echo signals were acquired, from a 40×40 mm^2 ROI (starting at a depth of 10 mm under the transducer) for applied strains ranging from 0.5 to 3% at steps of 0.5%.

We have implemented an automated beam-steering and data acquisition algorithm on the Ultrasonix system. The algorithm first acquires the precompression data along the specified angular sweep (0° to 15°) at 0.75° increments. The stepper motor is then activated to compress the phantom at a specified compression increment (0.5%), following which the post-compression RF data are acquired following the same angular scan sequence. In order to obtain statistically independent results, pre- and post-compression data were acquired over ten independent realizations along the different scanning planes and at different pre-compression levels.

Each of the angular pre- and post-compression RF frames acquired were analyzed separately to calculate the correlation coefficient at the specified angle. Cross-correlation analysis using a window size of 3 mm and 75% overlap of consecutive windows was used to generate the normalized cross-correlation function. The correlation coefficient is obtained from the peak of the normalized cross-correlation function.

B. Computation of the effective aperture

The actual aperture of the transducer during RF data acquisition was not available during the experiment. Therefore, we calculated the correlation between two parallel RF echo signal segments for the zero-angle frame to estimate the PSF of the system, which in turn would yield an effective aperture estimate.[36] We selected a 4 mm RF segment centered at a depth of 3 cm for each beam line and calculated the correlation coefficient value versus the beam line separation as shown in Fig. 4. The error bars denote the standard deviation of the mean estimates over 20 different lateral positions. Since the transmit focus is set to a depth of 1.0 cm with a dynamic receive focus, the transmit PSF at a 3-cm depth is significantly wider than the receive PSF. The combined PSF, a product of transmit and receive PSF, can be approximated by the receive PSF, which can be written as

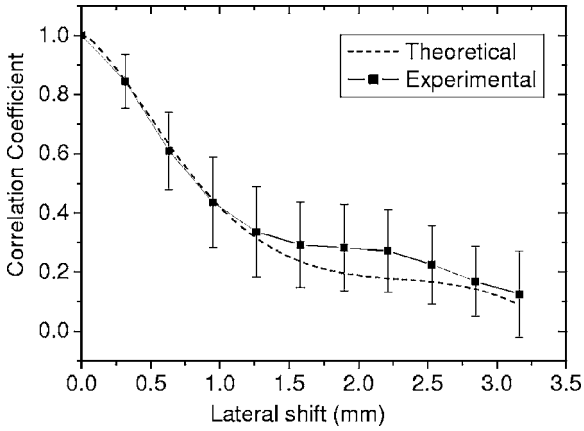

FIG. 4. Correlation coefficient for echo data obtained from parallel RF beam lines. The solid line is the measured correlation coefficient estimate and the dashed curve denotes the approximated theoretical curve generated by assuming a transducer aperture size of 8 mm.

$$p_x(x) = \sin(\pi f_0 x)/(\pi f_0 x). \tag{22}$$

Note the difference between Eqs. (22) and (8), where we assume that the transmit and receive foci are located at the same position as the origin of the echo signal; therefore, the PSF in that case would be the product of two identical sinc functions.

We use the method described by Chen *et al.*[36] to compute the correlation between two parallel beam lines and to determine the effective aperture. We estimated that for an effective receive aperture size of $D=8$ mm, the theoretical prediction fits the experimental data (Fig. 4), where the best fit curve is plotted as a dashed line. With this effective aperture size, we can predict the decorrelation of the pre- and post-compression RF signal segments with an increase of beam angle, and compare the theoretical predictions with the experimental data.

IV. RESULTS

To verify the accuracy of the proposed theory, we use experimental RF data to compute estimates of the correlation coefficient and to compare these results to the theoretical prediction. We selected a location in the phantom at a depth of 3 cm along the central beam line for a 0 deg insonification angle. For each subsequent insonification angle, we then locate the beam line that intersects or passes closest to that point and chose the RF data segment centered at that point. A rectangular window was used to segment or gate the RF data.

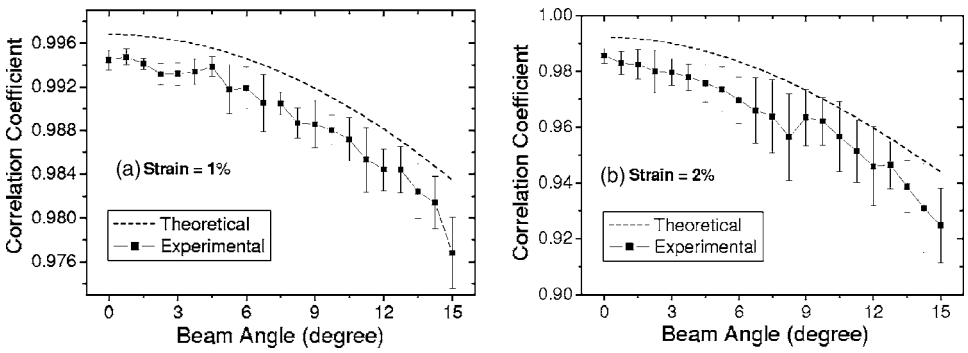

FIG. 5. Comparison between theoretical prediction and experimental results for the correlation coefficient of pre- and post-compression RF segments acquired at different beam angles. Results are shown for applied strains of (a) 1%, and (b) 2%. The correlation coefficient was obtained for a 5 MHz center frequency, using a 3-mm RF data segment centered at a depth of 3 cm.

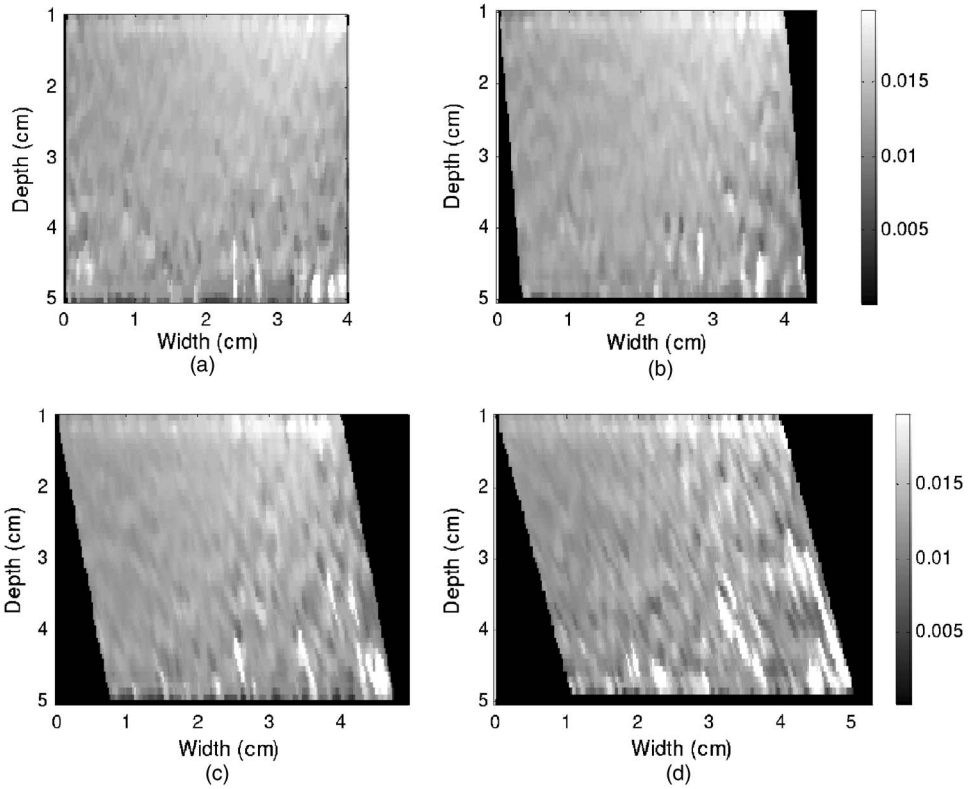

FIG. 6. Angular strain images obtained at (a) 0°, (b) 4.5°, (c) 10.5°, and (d) 15° angles under an applied strain of 1.5%. The colorbar denotes strain, where 1% strain is displayed as 0.01.

Since the window length was selected to be 3 mm and signal intensity variations due to attenuation and focusing effects are ignored, the window function $w(t)$ can be set to 1. The resultant correlation coefficient curves are plotted as a function of the beam angle in Fig. 5 for applied compressions of (a) 1% and (b) 2%. The error bars denote the standard deviation of the mean estimates over ten independent data sets. The theoretical prediction, obtained by numerically calculating Eq. (14), is plotted as a dashed line. Note that the theoretical curve is just above the errorbars of the experimental curve in most beam angle cases. This is because our theoretical model assumes that the displacement along the beam direction has been accurately tracked, in which case the correlation coefficient achieves the maximum value at that beam angle. The experimental estimates of the displacement, however, always contain errors due to the motion tracking algorithm and sampling precision. Therefore, the correlation coefficient obtained from experiment is lower than the theoretical prediction.

The reduction in the correlation coefficient with beam angle manifests as increased decorrelation errors leading to noisy estimation of the displacement and subsequently the local strain in the angular strain images. Examples of angular strain images obtained from the uniformly elastic phantom are shown in Fig. 6, for angles of 0°, 4.5°, 10.5°, and 15°. Note the presence of increased noise artifacts in the strain images with an increase in the insonification or beam angle.

V. DISCUSSION

Spatial-angular compounding can reduce noise artifacts in elastograms, but at the expense of the additional processing time required for displacement and strain estimations along angular directions. The most efficient spatial compounding procedure would be obtained by averaging independent, uncorrelated angular elastograms or strain estimates.[33] The effective number of independent strain estimates obtained depends on two factors: the angular incre-

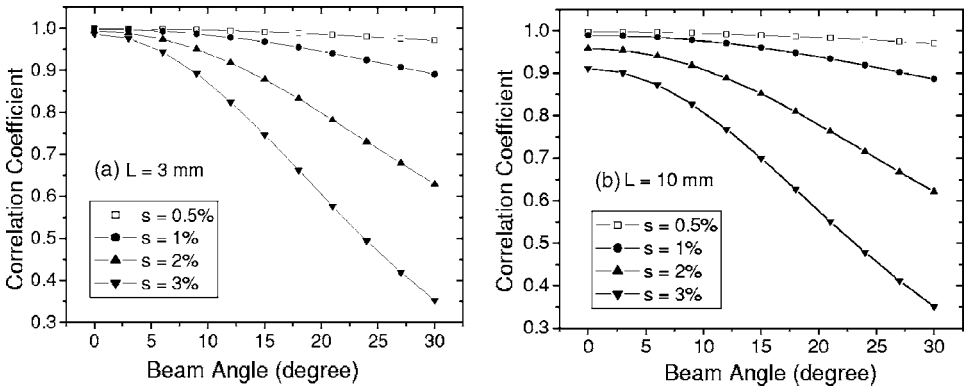

FIG. 7. Plots of the theoretical prediction of the correlation coefficient versus the beam angle for different applied strain and RF data segment lengths of (a) 3 mm and (b) 10 mm. The RF data segment was centered at a 3-cm depth.

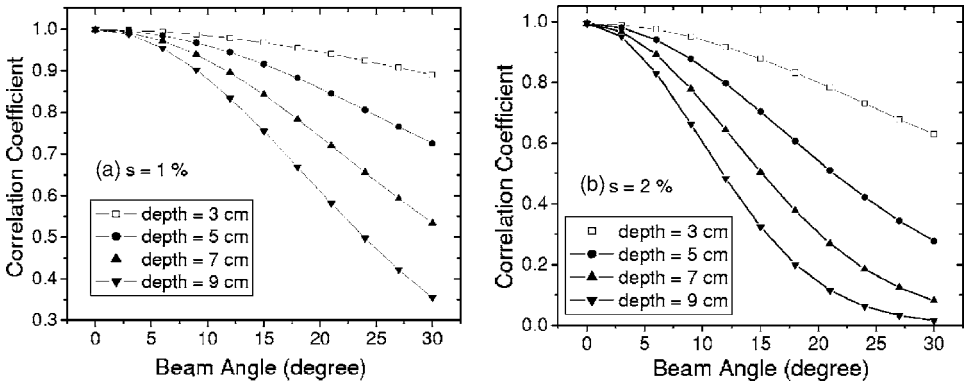

FIG. 8. Plots of the theoretical prediction of the correlation coefficient versus the beam angle for RF data segments obtained at different depths. Results are shown for applied strains of (a) 1%, and (b) 2%. A 3-mm RF segment length is used in the calculation.

ment and the maximum angle used for angular compounding. Generally, increasing the maximum angle for compounding reduces the strain variance and improves the SNRe. However, increased decorrelation noise artifacts are present for the elastograms obtained over larger insonification angles as illustrated in this paper. It is useful to understand how the beam angle and other system factors affect the correlation between pre- and post-compression signals.

Figure 7 shows approximated theoretical correlation coefficient curves as a function of beam angle using RF data segment lengths of (a) 3 mm, and (b) 10 mm, for applied strain values of 0.5, 1, 2, and 3 %, respectively. Here the RF data segment was assumed to be centered at a 3-cm depth in the phantom, and the aperture of the transducer was computed to be 1.5 cm. As illustrated in the figure, the decorrelation rate of the RF signal pairs increase with the value of the applied strain. This increased decorrelation rate is due to the fact that with increased strain more scatterers would leave the beam, leading to increased decorrelation, especially at the larger beam angles. Note that this is also the reason that the applied strain has a smaller effect on the correlation coefficient at smaller beam angles, as shown in Fig. 7. Variations in the correlation coefficient for different gated RF signal segment lengths are also observed in Figs. 7(a) and 7(b). As expected, when echo signals that are further away from the center of the initial data segment are included within the gated segment, increased signal decorrelation occurs between the pre- and post-compression signals. This effect is more pronounced for the smaller beam angles and reduces with an increase in the beam angle. This is due to the fact that at the larger beam angles the major contribution to the signal decorrelation comes from the scatterers moving out of beam and the effect of the data segment length alone appears to be negligible.

Figure 8 shows the theoretical prediction for the correlation coefficient curves for RF signals obtained at different depths. Results are shown for applied strains of (a) 1%, and (b) 2%. A 3-mm RF segment length was used in the calculation, and the aperture of the transducer was dynamically changed to enable the beam to be focused at the different depths. As expected, deeper segments of RF signals decorrelate more rapidly with corresponding increases in the beam angle. This result is explained by the geometric location of the scatterers and beam lines before and after compression, illustrated in Fig. 1. Considering the scatterers that contribute to the θ-angled RF segment centered at point O_1, after compression, these scatterers move to the locations centered at point O_1', which is essentially outside the beamwidth, leading to signal decorrelation. The distance that the scatterers move increases with both the depth and the applied strain. Therefore, the correlation coefficient decreases at a faster rate at deeper locations with larger applied strains. Note that an increased depth does not have an appreciable impact on signal decorrelation at the 0-deg beam angle since the scatterers remain within the beam as they are displaced or deformed along the axial direction.

Figure 9 shows plots of the correlation coefficient versus the beam angle for different insonification frequencies. Results are obtained using 3-mm RF segments centered at a depth of 3 cm for 1% applied strain. As illustrated in the figure, the signal decorrelation rate of RF signal pairs increases with the center frequency. This is primarily due to the fact that the ultrasound beam becomes narrower with the increased center frequency, enabling scatterers that were within the precompression beam to leave the beam and newer scatterers to come within the beam after compression when the beam becomes narrower, especially at larger beam angles. A similar increase in the decorrelation rate is observed when the aperture of the transducer is changed to obtain a narrower beam. Figure 10 plots the correlation coefficient curves for different transducer apertures for a 5 MHz center or insonification frequency. A 3-mm RF data segment centered at a 3-cm depth with 1% applied strain, is

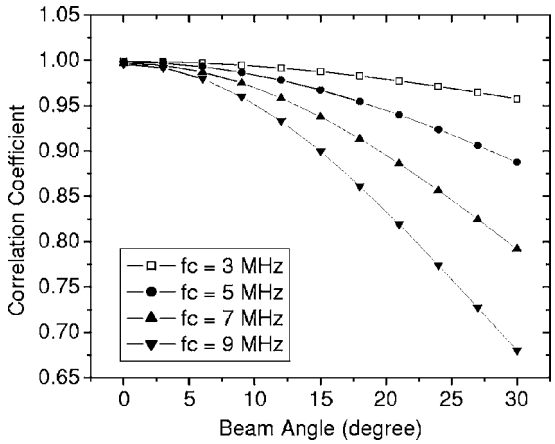

FIG. 9. Plots of the theoretical prediction of the correlation coefficient versus the beam angle for different center frequencies. Results are obtained using 3-mm RF segments centered at a depth of 3 cm for 1% applied strain, and a transducer aperture of 1.5 cm.

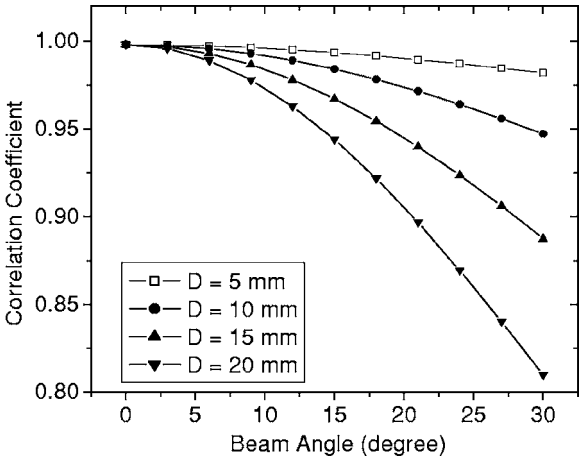

FIG. 10. Plots of the theoretical prediction of the correlation coefficient versus the beam angle for different transducer aperture sizes. Results are obtained using 3-mm RF segments centered at a depth of 3 cm for 1% applied strain, and a center frequency of 5 MHz.

utilized for Fig. 10. For larger apertures, the correlation coefficient curve falls off quickly with beam angle due to the narrower beam.

VI. CONCLUSIONS

A theoretical expression has been derived for the signal decorrelation between pre- and post-compression RF echo signals obtained at different angular insonifications, using beam steering to obtain angular elastograms. This work is based on previous theoretical results presented by Chen *et al.*,[36] where the analysis of the correlation between RF signals acquired from the same location but at different angles were presented. The analysis is extended to study the correlation between pre- and post-compression RF signals at a specified beam angle. The theoretical prediction matches well with the experimental results obtained using beam steering on a linear array transducer. The theoretical results derived in this paper is useful for evaluating the strain estimation performance of angular compounding and shear strain estimation using angular RF data[22,24] in elastography. For angular compounding and shear strain imaging, the theoretical results would enable the estimation of optimal maximum insonification angle to streamline the data processing. To find the optimum angular increment, more work is required to analyze the correlation between the angular elastograms obtained at different angles.

ACKNOWLEDGMENTS

This work is supported in part by NIH Grant No. R21 EB003853. The authors would also like to thank Dr. Laurent Pelissier for the loan of the Ultrasonix 500 RP system used on this research.

[1]J. Ophir, I. Cespedes, H. Ponnekanti, Y. Yazdi, and X. Li, "Elastography—A quantitative method for imaging the elasticity of biological tissues," Ultrason. Imaging **13**, 111–134 (1991).
[2]R. Muthupillai, D. J. Lomas, P. J. Rossman, J. F. Greenleaf, A. Manduca, and R. L. Ehman, "Magnetic-resonance elastography by direct visualization of propagating acoustic strain waves," Science **269**, 1854–1857 (1995).
[3]J. Ophir, S. K. Alam, B. Garra, F. Kallel, E. Konofagou, T. Krouskop, and T. Varghese, "Elastography: Ultrasonic estimation and imaging of the elastic properties of tissues," Proc. Inst. Mech. Eng., Part H: J. Eng. Med. **213**, 203–233 (1999).
[4]T. Varghese, J. Ophir, E. Konofagou, F. Kallel, and R. Righetti, "Tradeoffs in elastographic imaging," Ultrason. Imaging **23**, 216–248 (2001).
[5]A. Pesavento, A. Lorenz, S. Siebers, and H. Ermert, "New real-time strain imaging concepts using diagnostic ultrasound," Phys. Med. Biol. **45**, 1423–1435 (2000).
[6]I. Cespedes, J. Ophir, H. Ponnekanti, and N. Maklad, "Elastography: Elasticity imaging using ultrasound with application to muscle and breast in vivo," Ultrason. Imaging **15**, 73–88 (1993).
[7]M. O'Donnell, A. R. Skovoroda, B. M. Shapo, and S. Y. Emelianov, "Internal displacement and strain imaging using ultrasonic speckle tracking," IEEE Trans. Ultrason. Ferroelectr. Freq. Control **41**, 314–325 (1994).
[8]K. J. Parker, S. R. Huang, R. A. Musulin, and R. M. Lerner, "Tissue response to mechanical vibrations for sonoelasticity imaging," Ultrasound Med. Biol. **16**, 241–246 (1990).
[9]M. Bertrand, M. Meunier, M. Doucet, and G. Ferland, "Ultrasonic biomechanical strain gauge based on speckle tracking," *IEEE Ultrasonics Symposium* (Montreal, Quebec, Canada, 1989) pp. 859–864.
[10]T. A. Krouskop, D. R. Dougherty, and F. S. Vinson, "A pulsed Doppler ultrasonic system for making noninvasive measurements of the mechanical properties of soft tissue," J. Rehabil. Res. Dev. **24**, 1–8 (1987).
[11]M. F. Insana, L. T. Cook, M. Bilgen, P. Chaturvedi, and Y. Zhu, "Maximum-likelihood approach to strain imaging using ultrasound," J. Acoust. Soc. Am. **107**, 1421–1434 (2000).
[12]K. Nightingale, M. Scott Soo, R. Nightingale, and G. Trahey, "Acoustic radiation force impulse imaging: in vivo demonstration of clinical feasibility," Ultrasound Med. Biol. **28**, 227–235 (2002).
[13]A. Pesavento, A. Lorenz, S. Siebers, and H. Ermert, "New real-time strain imaging concepts using diagnostic ultrasound," Phys. Med. Biol. **45**, 1423–1435 (2000).
[14]D. B. Plewes, I. Betty, S. N. Urchuk, and I. Soutar, "Visualizing tissue compliance with MR imaging," J. Magn. Reson Imaging **5**, 733–738 (1995).
[15]E. Konofagou and J. Ophir, "A new elastographic method for estimation and imaging of lateral displacements, lateral strains, corrected axial strains and Poisson's ratios in tissues," Ultrasound Med. Biol. **24**, 1183–1199 (1998).
[16]E. E. Konofagou and J. Ophir, "Precision estimation and imaging of normal and shear components of the 3D strain tensor in elastography," Phys. Med. Biol. **45**, 1553–1563 (2000).
[17]U. Techavipoo, Q. Chen, T. Varghese, and J. A. Zagzebski, "Estimation of displacement vectors and strain tensors in elastography using angular insonifications," IEEE Trans. Med. Imaging **23**, 1479–1489 (2004).
[18]S. K. Alam, J. Ophir, and E. E. Konofagou, "An adaptive strain estimator for elastography," IEEE Trans. Ultrason. Ferroelectr. Freq. Control **45**, 461–472 (1998).
[19]S. K. Alam and J. Ophir, "Reduction of signal decorrelation from mechanical compression of tissues by temporal stretching: Applications to elastography," Ultrasound Med. Biol. **23**, 95–105 (1997).
[20]I. Cespedes and J. Ophir, "Reduction of image noise in elastography," Ultramicroscopy **15**, 89–102 (1993).
[21]T. Varghese, J. Ophir, and I. Cespedes, "Noise reduction in elastograms using temporal stretching with multicompression averaging," Ultrasound Med. Biol. **22**, 1043–1052 (1996).
[22]U. Techavipoo and T. Varghese, "Wavelet denoising of displacement estimates in elastography," Ultrasound Med. Biol. **30**, 477–491 (2004).
[23]U. Techavipoo and T. Varghese, "Improvements in elastographic contrast-to-noise ratio using spatial-angular compounding," Ultrasound Med. Biol. **31**, 529–536 (2005).
[24]U. Techavipoo, Q. Chen, T. Varghese, J. A. Zagzebski, and E. L. Madsen, "Noise reduction using spatial-angular compounding for elastography," IEEE Trans. Ultrason. Ferroelectr. Freq. Control **51**, 510–520 (2004).
[25]M. Rao, Q. Chen, H. Shi, and T. Varghese, "Spatial-angular compounding for elastography using beam steering on linear array transducers," Med. Phys. **33**, 618–626 (2006).
[26]J. Meunier and M. Bertrand, "Ultrasonic texture motion analysis—Theory and simulation," IEEE Trans. Med. Imaging **14**, 293–300 (1995).
[27]M. Bilgen and M. F. Insana, "Deformation models and correlation analysis in elastography," J. Acoust. Soc. Am. **99**, 3212–3224 (1996).
[28]F. Kallel and J. Ophir, "Three-dimensional tissue motion and its effect on

image noise in elastography," IEEE Trans. Ultrason. Ferroelectr. Freq. Control **44**, 1286–1296 (1997).
[29]T. Varghese, M. Bilgen, and J. Ophir, "Multiresolution imaging in elastography," IEEE Trans. Ultrason. Ferroelectr. Freq. Control **45**, 65–75 (1998).
[30]M. Bilgen, "Dynamics of errors in 3D motion estimation and implications for strain-tenser imaging in acoustic elastography," Phys. Med. Biol. **45**, 1565–1578 (2000).
[31]R. F. Wagner, M. F. Insana, and S. W. Smith, "Fundamental correlation lengths of coherent speckle in medical ultrasonic images," IEEE Trans. Ultrason. Ferroelectr. Freq. Control **35**, 34–44 (1988).
[32]R. F. Wagner, S. W. Smith, J. M. Sandrik, and H. Lopez, "Statistics of speckle in ultrasound B-scans," IEEE Trans. Sonics Ultrason. **30**, 156–163 (1983).
[33]M. Odonnell and S. D. Silverstein, "Optimum displacement for compound image generation in medical ultrasound," IEEE Trans. Ultrason. Ferroelectr. Freq. Control **35**, 470–476 (1988).
[34]S. W. Smith, R. F. Wagner, J. M. Sandrik, and H. Lopez, "Low contrast detectability and contrast detail analysis in medical ultrasound," IEEE Trans. Sonics Ultrason. **30**, 164–173 (1983).
[35]C. B. Burckhardt, "Speckle In Ultrasound B-Mode Scans," IEEE Trans. Sonics Ultrason. **25**, 1–6 (1978).
[36]Q. Chen, A. L. Gerig, U. Techavipoo, J. Zagzebski, and T. Varghese, "Correlation of RF Signals During Angular Compounding," IEEE Trans. Ultrason. Ferroelectr. Freq. Control **52**, 961–970 (2005).
[37]E. L. Madsen, G. R. Frank, T. A. Krouskop, T. Varghese, F. Kallel, and J. Ophir, "Tissue-mimicking oil-in-gelatin dispersions for use in heterogeneous elastography phantoms," Ultrason. Imaging **25**, 17–38 (2003).